

# Broadband Linear-Dichroic Photodetector in a Black Phosphorus Vertical p-n Junction

Hongtao Yuan,<sup>1,2</sup> Xiaoge Liu,<sup>1</sup> Farzaneh Afshinmanesh,<sup>1</sup> Wei Li,<sup>1</sup> Gang Xu,<sup>1</sup> Jie Sun,<sup>1</sup> Biao Lian,<sup>1</sup> Alberto G. Curto,<sup>1</sup> Guojun Ye,<sup>3</sup> Yasuyuki Hikita,<sup>1,2</sup> Zhixun Shen,<sup>1,2</sup> Shou-Cheng Zhang,<sup>1,2</sup> Xianhui Chen,<sup>3</sup> Mark Brongersma,<sup>1,2</sup> Harold Y. Hwang,<sup>1,2\*</sup> Yi Cui<sup>1,2\*</sup>

<sup>1</sup>*Geballe Laboratory for Advanced Materials, Stanford University, Stanford, California 94305, USA*

<sup>2</sup>*Stanford Institute for Materials and Energy Sciences, SLAC National Accelerator Laboratory, Menlo Park, California 94025, USA*

<sup>3</sup>*Hefei National Laboratory for Physical Science at Microscale and Department of Physics, University of Science and Technology of China, Hefei, Anhui 230026, China*

The ability to detect light over a broad spectral range is central for practical optoelectronic applications, and has been successfully demonstrated with photodetectors of two-dimensional layered crystals such as graphene and MoS<sub>2</sub>. However, polarization sensitivity within such a photodetector remains elusive. Here we demonstrate a linear-dichroic broadband photodetector with layered black phosphorus transistors, using the strong intrinsic linear dichroism arising from the in-plane optical anisotropy with respect to the atom-buckled direction, which is polarization sensitive over a broad bandwidth from about 400 nm to 3750 nm. Especially, a perpendicular built-in electric field induced by gating in the transistor geometry can spatially separate the photo-generated electrons and holes in the channel, effectively reducing their recombination rate, and thus enhancing the performance for linear dichroism photodetection. This provides practical functionality using anisotropic layered black phosphorus, thereby enabling novel optical and optoelectronic device applications.

---

\* Corresponding author: [hyhwang@stanford.edu](mailto:hyhwang@stanford.edu), [yicui@stanford.edu](mailto:yicui@stanford.edu).

Confined electronic systems in layered two-dimensional (2D) crystals are host to many emerging electronic, spintronic and photonic phenomena,<sup>1, 2, 3</sup> including quantum Hall and Dirac electrons in graphene<sup>4, 5, 6</sup> and topological surface states in topological insulators<sup>7, 8</sup>. Experimentally identifying new functionalities of two-dimensional materials is a challenging and rewarding frontier, enabled by recent advances in materials and device fabrication. One example is the valley polarization control using circularly polarized light in the non-centrosymmetric MoS<sub>2</sub> monolayer and resulting potential valleytronics applications.<sup>9, 10, 11</sup> Other examples include recent demonstrations of novel electronic and optoelectronic applications of the well-known layered material black phosphorus (BP), such as high-mobility field effect transistors and linear-polarization dependent optical absorption.<sup>12,13,14</sup> Therefore, further discovering new properties and functionalities utilizing known layered materials is of practical importance and great current interest.<sup>14, 15, 16, 17, 18, 19, 20, 21, 22, 23, 24, 25, 26</sup>

As a potential functionality for layered 2D materials, linear dichroism (LD) is an electromagnetic spectroscopy probing different absorption of light polarized parallel or perpendicular to an orientation axis. It directly depends on the conformation and orientation of material/device structures, where they are either intrinsically oriented in an anisotropic crystal structure<sup>27, 28</sup> or extrinsically oriented in anisotropic device patterns<sup>29, 30</sup>. Compared to the hexagonal in-plane lattice in other 2D materials such as graphene and MoS<sub>2</sub>, which are insensitive to the linear polarization of incident light, the layered BP crystal with a rectangular in-plane lattice has a highly-anisotropic structure along the  $x$  and  $y$  directions (defined in Fig. 1a), where every two rows of P atoms alternately puckers up and down to form an “armchair”-like geometry only along the  $x$  direction. Therefore the electrons and photons in BP can behave in a highly anisotropic manner within the layer plane.<sup>18, 19</sup> In contrast to existing photodetectors for linear dichroism detection based on extrinsic geometric effects such as with wire-grid patterns,<sup>30, 31, 32, 33</sup> BP with a mirror reflection symmetry only in the  $y$  direction (Supplementary Fig. S1a) offers an exciting opportunity to incorporate intrinsic crystal anisotropy for linear-polarization-sensitive photodetection. In this Article, we demonstrate a linear dichroic photodetector based on BP transistors, where the polarized light is absorbed differently along two in-plane crystal axes across a very broad spectral range from about 400 nm to 3750 nm. The optical selection rules in BP allow the broad-band absorption of the light

polarized preferential in the  $x$  direction, and leads to a new degree of freedom to control/manipulate electronic and optoelectronic properties in layered BP. In particular, utilizing the vertical p-n junction induced by an ionic gel gated transistor, we spatially separate the photo-generated electron-hole pairs in the channel, reducing their recombination rate and thus enhancing the photoresponsivity of the photodetector.

Similar to the layered structure of other 2D materials, BP is composed of stacking the monolayer structure (four-formula  $P_4$  block unit) along the  $z$ -axis (Fig. 1a). Different from the layered crystals with  $sp^2$  bonding and a flat in-plane lattice, the BP monolayer, puckered along the  $x$  direction due to the  $sp^3$  hybridization, creates an anisotropic band structure. We performed angle resolved photoemission spectroscopy (ARPES) and theoretical band calculations to study the structure of the band dispersion anisotropy of BP. In the experimental band structure obtained by ARPES (Figs. 1c and 1d), the valence band maximum of bulk BP resides at the Z point, the center of the  $k_z = \pi$  plane in the Brillouin zone (Fig. 1b).<sup>34</sup> Furthermore, the bands along Z-L ( $k_x$ ) and Z-P ( $k_y$ ) directions have different evolving slopes. The elliptic pockets in the constant energy contours (Fig. 1d) directly reflect the anisotropic effective mass and free carrier velocity along the two perpendicular in-plane directions. Band calculations clearly indicate a direct band gap of 0.33 eV for bulk BP. The direction with small effective masses ( $0.12 m_0$  for holes and  $0.11 m_0$  for electrons) is the  $k_x$  direction (the puckering  $x$  direction in real-space). In contrast, the valence (conduction) band along the  $k_y$  direction is a relatively flat band and gives a larger hole (electron) effective mass of about  $0.81 m_0$  ( $1.3 m_0$ ), reflecting a large electronic anisotropy along Z-P and Z-L directions (Fig. 1c).<sup>12</sup> Considering the orbital component within this  $sp^3$  hybridization (partial density of states shown in Fig. 1e), the band dispersions near the valence band maximum and the resulting band gap mainly originate from the  $p_z$  orbital localized along the  $z$  direction.

A symmetry analysis from the band structure for the optical selection rules can explain why and how BP exhibits linear dichroism and anisotropic absorption along the two perpendicular planar directions. As shown in Supplementary Fig. S1a, the BP crystal structure possesses inversion symmetry (parity) and mirror reflection symmetry ( $M_y$ ) only in the  $y$  direction. Electron states at high symmetry points (*e.g.*, Z,  $\Gamma$ ) in the Brillouin Zone can thus be labeled by these two

symmetries, and correspondingly there are two optical selection rules: 1) Parity selection rule: Since the photons carry parity  $-1$ , the first optical selection rule is that the optical absorption by an electron can only occur between electron states (bands) with opposite parities; 2) Polarization selection rule: This rule concerns the polarization of the normally incident light: Under mirror reflection ( $M_y$ ), the field of polarized light ( $E_y$ ) in  $y$ -direction changes sign ( $E_y \rightarrow -E_y, B_x \rightarrow -B_x$ ), while that of polarized light ( $E_x$ ) in  $x$ -direction is unchanged ( $E_x \rightarrow E_x, B_y \rightarrow B_y$ ). Therefore, the absorption of the  $x$ -direction ( $y$ -direction) polarized light is only allowed between electron states with the same (opposite) eigenvalue of  $M_y$  (for example,  $+1$  or  $-1$ ). We note that the second rule applies also for all electron states in the  $y$ -direction momentum  $k_y = 0$  plane.

According to the optical selection rules, we find the lowest energy optical transition in BP occurs at the Z point across the gap ( $\sim 0.33$  eV) between the valence band Vb1 and the conduction band Cb1 with opposite parities (Fig. 2a).<sup>27</sup> Both bands have  $M_y = +1$  at Z point and in the  $k_y = 0$  plane. The electron states in the  $k_y = 0$  plane (Z-L direction in Fig. 2a) are therefore forbidden to absorb light polarized in the  $y$ -direction. In contrast, states in the  $k_x = 0$  plane (Z-P direction in Fig. 2a) in general have no  $M_y$  symmetry, and thus the absorption of both  $x$ - and  $y$ -direction polarized light is symmetry allowed. Overall, the absorption of polarized light in  $y$ -direction is forbidden at 0.33 eV and also significantly reduced at higher energies, which leads to linear polarization dependent absorption spectrum in BP. Note that the pair of bands Vb1 $\leftrightarrow$ Cb1 can contribute to the intrinsic light absorption in a broad range of photon energy from 0.33 eV to 4 eV, and thus supports a wide continuous polarization dependent absorption spectrum. However, optical absorption channels between other bands will be involved for photon energies above 1.2 eV, where the polarization-sensitivity is either weakened or strengthened. Based on the band structure calculations (Fig. 2a), we find that all the photon absorption channels up to around 3.0 eV favor the absorption of  $x$ -polarized light, while the band pairs of Vb3-Cb1 and Vb1-Cb4 favoring  $y$ -polarized light are involved in absorption processes above 3.0 eV (see Fig. 2a and Supplementary Section 3). Therefore, in principle the polarization dependence of the absorption continuously covers a wide range from 0.33 eV up to  $\sim 3.0$  eV (3750 nm – 400 nm in wavelength).

To experimentally verify the linear dichroism of BP, we performed polarization dependent

absorption and reflection measurements on cleaved BP flakes (details are given in Supplementary Section 3). The crystal orientation of mechanically-cleaved BP samples is investigated by systematic studies using high-resolution transmission electron microscopy (Supplementary Section 1). In the infrared (IR) regime (Fig. 2b), the reflection spectrum with the incident light polarized along the  $x$ -axis of the BP crystal has a sudden drop with photon energies larger than the band gap (0.33 eV) of BP. In contrast, the reflection of light polarized along the  $y$ -axis shows no decrease near the band edge. One can clearly see the gradual evolution of the reflection spectra (from 30% to ~90%) using light with changing polarization angles from  $x$  to  $y$  directions. This implies that more photons are absorbed with incident light polarized along the  $x$ -axis relative to the case with light polarized along the  $y$  axis, consistent with our theoretical analysis and recent optical studies.<sup>12,18, 19</sup> Similar polarization dependent phenomena are observed for visible light (Fig. 2c); the transmittance with the light polarized along the  $x$ -axis is low (42% at 2.3 eV) and the flake appears darker with more absorption (inset of Fig. 2c). By contrast, when light is polarized along the  $y$ -axis, the transmittance at 2.3 eV is as high as 80%, and the flake appears transparent. A video in the Supplementary Information clearly indicates the gradual changes of the transmittance during continuous rotation of the polarization axis. Such a linear dichroism is consistent with recent reports on the linear polarization dependent absorption in BP flakes.<sup>12,18, 19</sup>

The polarization dependent anisotropic absorption in BP can be further reflected by its photoconductivity. Scanning photocurrent microscopy was performed using a supercontinuum Fianium laser (400-1700 nm in wavelength) to measure the spatially dependent photoresponse of BP devices (first on a Hall-bar patterned BP device as shown in Supplementary Section 4). A small DC voltage ( $V_{SD} = 0.1$  V) is applied between the source-drain electrodes (Supplementary Fig. S4b). As shown in the large-area photocurrent scanning image for the whole channel (Supplementary Fig. S4c), one can see the strong signal of the photocurrent  $|I_{ph}|$  at two different BP/metal electrode edges and zero photoresponse in the center area of the flake far from electrodes. Supplementary Fig. S4d shows the evolution of photocurrent mapping images ( $|I_{ph}|$ ) at a constant wavelength of 1500 nm as a function of the polarization angle of the incident light, with the laser spot scanning near the metal electrode edges (indicated by the yellow square in Supplementary Fig. S4c). The photocurrent is

maximum by showing a strip shape when the incident light is polarized along the  $x$  crystal axis (defined as  $0^\circ$  polarization) and is minimum when the incident light is polarized along the  $y$  crystal axis (defined as  $90^\circ$  polarization), directly indicating the polarization dependent absorption and the resulting linear dichroic photocurrent generation. Note that the photocurrent at two different BP/metal electrode edges has opposite flowing directions (more details are given in Supplementary Fig. S8) and there is a zero photocurrent crossover along the channel. Such a current flow profile and the zero-photocurrent crossing along the current channel can be ascribed to the photo thermoelectric effect under pulsed excitation heating rather than the photovoltaic effects originating from the built-in electric field between the source/drain electrodes. Our systematic measurements indicate that the photo thermoelectric effect dominates the photocurrent generation at zero and low DC voltages ( $|V_{SD}| < 0.15$  V) while the photo-voltaic effect starts to dominate the photocurrent process at higher  $|V_{SD}|$ . More details are given in Supplementary Section 6.

To exclude the possibility that the observed two-fold polarization dependent photocurrent originates from a geometric edge effect at the metal/BP edge, we designed a “ring”-shaped metal electrode as the photocurrent collector (Fig. 3a), in which the photogenerated hot carriers can be collected isotropically where the influence from the orientation of the electrode edge is the same for all polarizations. A small DC voltage ( $V_{SD} = 0.1$  V) is applied between the source-drain electrodes so the device works in the photo thermoelectric regime, aiming to see the intrinsic behavior from the anisotropic BP flakes without the photocurrent driven by an external electric field in the photovoltaic regime. Figure 3b shows the full spatial mapping of the photocurrent around the ring electrode at a wavelength of 1500 nm. Focusing the excitation in the round area within the inner diameter of the “ring” electrode, the photocurrent with  $0^\circ$  light polarization ( $x$  crystal axis) is much larger than that for  $90^\circ$  light polarization (Fig. 3c), suggesting that the intrinsic polarization dependent photoresponse originates from BP itself. The photoresponsivity (photocurrent normalized to the incident laser power) at 1200 nm is as large as 0.35 mA/W and also has a large contrast ratio (3.5) between the photoresponsivity along the two perpendicular polarizations.

These observations clearly indicate that the incident light in different polarization states travelling through the dichroic BP experiences a varying absorption, directly reflecting the intrinsically

anisotropic conformation and orientation of the crystal structure. Related to the total intrinsic vertical optical transition for a single pair of bands ( $Vb1 \leftrightarrow Cb1$  transition mentioned above for Fig. 2a), the photoresponsivity to polarized laser excitation with varying wavelength range from 400 nm to 1700 nm directly indicates the wide bandwidth of the linear dichroism detection (Fig. 3c). Compared to reported linear dichroism applications based on a wire-grid polarizer,<sup>30,31</sup> which have largely relied on advances in nanofabrication, our observations on the linear dichroism photodetection demonstrate that layered BP can be used as a potential intrinsic linear dichroism media with broad-band response for practical integrated optical applications. Also interestingly, by combining the highly efficient polarization dependent optical absorbing characteristics with the good transport characteristics, BP could be a promising material for high performance optoelectronic devices. Its relatively small carrier effective masses along the  $x$  and  $z$  direction give a carrier mobility an order of magnitude larger than typical perovskite absorbers<sup>35,36</sup> and layered chalcogenides<sup>16,37</sup>. Consequently, the large carrier mobility directly affects the photoresponse speed of the BP photodetector devices. As indicated in Supplementary Section 7, the photoresponse rise time of the linear dichroic BP photodetector can be faster than 40 micro-seconds ( $\mu s$ ), the detectable time-resolution limitation of the preamplifier in our photocurrent measurement setup. This value of 40  $\mu s$  is clearly faster than the photoresponse time of previously reported photodetector based on layered chalcogenides (normally in the order of milliseconds or even slower)<sup>16,37</sup>.

To enhance the performance of the BP photodetector, we formed the BP flakes into an ionic gel gated electric-double-layer transistor (EDLT), which has been known to be a powerful tool to tune interfacial band bending (perpendicular electric field) and also the Fermi level of channel materials over a large range.<sup>38, 39, 40</sup> Figures 4a and 4b show the ambipolar transfer characteristics, the source-drain current  $I_{DS}$  and sheet resistance  $R_s$  as functions of gate voltage ( $V_G$ ) for the BP-based EDLT. As a normally-ON transistor with a p-type channel, negative  $V_G$  accumulates holes at the gel/BP interface with upward band bending. Positive  $V_G$  first depletes the holes away from the interface and with further increase of  $V_G$ , an electron inversion layer can be induced (Supplementary Section 8). Hall effect measurements (Figs. 4c and 4d) clearly indicate the ambipolar operation in the channel, with the transition from hole conduction to electron conduction as  $V_G$  increases from zero to

a positive value. Carriers are confined at the gel/BP interface with a maximum attainable sheet carrier density up to  $1.2 \times 10^{14} \text{ cm}^{-2}$  for electrons and  $0.57 \times 10^{14} \text{ cm}^{-2}$  for holes, corresponding to a Fermi level shift of  $\sim 0.49 \text{ eV}$  above the conduction band minimum for electron accumulation, and of  $\sim 0.57 \text{ eV}$  below the valence band maximum for hole accumulation (estimated by the density of states of BP from band calculations). A qualitative estimation of the carrier distribution profile of the downward band bending case under a positive  $V_G$  indicates that electrons are strongly confined at the surface, while holes are distributed in the deeper bulk regime (Figs. 4f and 4g). Interestingly, the formation of the inversion layer (surface electron accumulation) on the p-type BP channel (holes in bulk) indicates that we can easily induce a vertical p-n junction structure within such an EDLT configuration. More importantly, the depth of the depletion layer and resulting p-n junction depth can be tuned with both the external perpendicular electric field (gate voltage) and the bulk carrier density in BP crystals, providing us with freedom for a rational control of the p-n junction for performance enhancement of BP photodetectors.

To this end, we vary the gate voltage  $V_G$  and show the corresponding photocurrent images of the BP ring pattern under various  $V_G$  (Figs. 5a-5c). With increasing  $V_G$  from zero bias to 1.5 V, the maximum photocurrent under the light irradiation (1500 nm) at  $0^\circ$  polarization dramatically increases and the photocurrent generation areas enlarge, while the photocurrent under the polarized light at  $90^\circ$  does not significantly change with varying  $V_G$ . As indicated in Figs. 5d and 5e, the photoresponsivity at 1700 nm ( $0^\circ$  polarization) can be one order of magnitude enhanced by applying a positive gate voltage, and correspondingly the ratio of the photoresponsivities between the two polarizations is greatly enhanced. The downward band bending and the resulting built-in perpendicular electric field in the BP channel in the vertical p-n junction can serve to spatially separate the photo-generated carriers (as schematically shown in the inset of Fig. 4e). Electrons move at the outmost surface while the holes move in the bulk. As the most direct result, the recombination probability between hot electrons/holes during their motion to opposite electrodes can be greatly reduced.<sup>41, 42, 43, 44</sup>

To generate the photocurrent, the mobile carriers will move to the electrode from the light spot center with exponential decay due to losses such as carrier recombination:



$$n(r) = n_0 e^{-\frac{r}{L_0}},$$

where  $r$  is the distance from the light spot center,  $L_0$  is the diffusion length and  $n_0$  is the number of generated electron-hole pairs by the light shining on the sample with intensity  $I_0$ . Therefore two factors can directly influence the photocurrent generation:  $L_0$  and  $n_0$ . Experimentally, if comparing the absolute distance from the BP/metal edge (20  $\mu\text{m}$  in Fig. 5f) to the position at a specific photocurrent level (10 nA), one can see that a higher  $V_G$  exhibits a long distance for the lateral diffusion of hot carriers, from 1.2  $\mu\text{m}$  for zero  $V_G$ , 2.2  $\mu\text{m}$  for 1.0 V, to 3.7  $\mu\text{m}$  for 1.5 V. However, there is almost no change in the normalized photocurrent by the maximum value at each  $V_G$ . This implies that the carrier diffusion length is not significantly changed with  $V_G$  and not the dominant mechanism for the photocurrent enhancement. Rather, it appears that the enhancement of  $n_0$  starts to be the key point for the absolute value increase in photocurrent. Namely, as the  $V_G$  increases, the tunable perpendicular electric field can separate the electrons and holes: electrons move on the surface and holes move in the bulk, which can reduce their recombination and increase the  $n_0$  value.

In contrast to conventional phototransistors, photogenerated electrons and holes in our vertical p-n junction structure are separated by selectively driving them into surface or bulk layers under the built-in electric field within the EDLT, which can minimize the hot carrier recombination. Therefore, this vertical p-n junction configuration can greatly enhance the efficiency of the linear dichroism photodetector. While far from optimized, our observations provide the first demonstration that a vertical p-n junction device structure can be significant for performance enhancement in the linear dichroism photodetection scheme using BP. Key to this approach is the direct combination of the intrinsic broadband linear dichroism of BP with its high mobility semiconductor characteristics, which can enable novel integrated optical and optoelectronic device applications beyond conventional materials and approaches.

## Methods

## Device fabrication of BP photodetector

Hall bar patterns and ring-shaped patterns with Ti/Au electrodes were fabricated on tape-cleaved BP single crystal flakes (on SiO<sub>2</sub>/Si wafer), which typically have dimensions of tens of micrometers laterally and a thickness of 30-50 nm. The bulk BP crystal shows the typical p-type conduction with carrier density in the order of  $10^{18} \text{ cm}^{-3}$ . The ring pattern is designed to exclude the possibility that the observed polarization-dependent absorption might originate from anisotropic scattering from the BP/metal edge. Serving as the side gate electrode for gel gated transistors, a large-area Ti/Au pad was deposited near the BP, but electrically insulated from the BP flake. A typical EDL transistor was fabricated by spin-coating DEME-TFSI-based ionic gel<sup>35</sup> [DEME-TFSI, N,N-diethyl-N-(2-methoxyethyl)-N-methylammonium bis-trifluoromethylsulfonyl-imide from Kanto Chemical Co]. Note that the ionic gel is transparent within the spectral regime from 300 nm to 3100 nm, covering the optical measurement regime (400-1700 nm). Transfer characteristics, longitudinal sheet resistance  $R_s$ , and Hall coefficient of Hall bar patterned devices were simultaneously measured in a liquid helium cryostat with a 14 T superconducting magnet.

## Optical measurements and scanning photocurrent microscopy

Optical reflectance and transmittance spectral measurements were carried out under ambient conditions at room temperature for samples on transparent quartz substrates. The spectra in the visible regime (1.5-3.0 eV) were obtained with a confocal scanning microscope (Nikon LV-UDM) equipped with a halogen lamp, a grating spectrometer and a CCD camera. The detection area was with a spot diameter of 10  $\mu\text{m}$ . For reflection measurements in the infrared, we used a Nicolet 6700 Fourier-transform infrared (FTIR) spectrometer equipped with a Continuum XL microscope (Thermo Electron Corp.). The IR light source was focused by a 15 $\times$  Cassegrain objective with angles ranging from 16 to 35.5 degree with respect to the sample normal. A variable knife-edge aperture located within the image plane is used to define the sample collection area, which is fixed in size to  $\sim 200 \mu\text{m} \times 200 \mu\text{m}$ . The spectral range was  $650\text{-}6500 \text{ cm}^{-1}$  (0.08~0.8 eV) with a resolution of  $4 \text{ cm}^{-1}$ . All spectra are the average of 32 scans. The reflectance spectra were plotted as  $(R_{\text{sample}}/R_{\text{Au}}) \times 100\%$ , where  $R_{\text{sample}}$  was collected from an area with a sample present and  $R_{\text{Au}}$  was collected from an adjacent Au pad as a total reflection mirror.

In photocurrent measurements, optical radiation of a well-defined wavelength is selected from a supercontinuum Fianium white light laser source using acousto-optic tunable filters. The laser beam passes through a linear polarizer and a half-wave plate and is then focused on the detector using a microscope objective (50×, 0.42 NA). The laser beam is modulated with a mechanical chopper (1 KHz) and the modulated photocurrent signal is amplified and detected using a lock-in technique. The photodetector device is mounted on a piezoelectric stage and a photocurrent image of the detector is obtained by raster scanning the laser beam over it. To investigate the time response of the detector, we illuminate it instead with an electrically modulated diode laser at 780 nm (Toptica DL-100), driven by a square wave function generator. After passing through a preamplifier, the photodetector signal is recorded in time by a digital oscilloscope.

### **ARPES and *ab initio* band calculations**

High-resolution ARPES experiments for cleaved BP samples were performed at the Synchrotron Radiation Light Source Beamline 5-4 under a base pressure better than  $3 \times 10^{-11}$  Torr, using incident photon energies of 19.5 eV with energy resolution of 12.5 meV and angular resolution of 0.2°. Electronic structure calculations were carried out by using the Vienna Ab-initio Simulation Package (VASP)<sup>45, 46</sup> based on experimental lattice constants and optimized internal parameters with accuracy smaller than 0.01 eV/Å. Perdew-Burke-Ernzerhof-type generalized gradient approximation<sup>47,48</sup> with MBJ correction was used to obtain an accurate semiconducting gap. The k-mesh for self-consistent calculations is  $12 \times 12 \times 16$ , and the cut-off energy is fixed to 400 eV.

### **Author Contribution**

H.T.Y., H.Y.H. and Y.C. conceived and designed the experiments. H.T.Y. performed sample fabrication and transport measurements. H.T.Y., X.G.L., F.A., A.G.C. and M.B. performed optical measurements. W.L. and Z.X.S. performed ARPES measurement. G.X., B.L. and S.C.Z. performed DFT calculations and theoretical analyses. X.G.L performed the band bending calculation. J.S. performed TEM analysis. G.J.Y and X.H.C. grew the high quality BP crystals. Y.H., M.B., Z.X.S., S.C.Z., X.H.C., H.Y.H. and Y.C. supervised the project and all authors contributed to data

discussions. H.T.Y. wrote the manuscript with input from all authors.

## **Acknowledgements**

This work was supported by the Department of Energy, Office of Basic Energy Sciences, Division of Materials Sciences and Engineering, under contract DE-AC02-76SF00515. B.L., G.X., H.Y.H. and S.C.Z. also acknowledge FAME, one of six centers of STARnet, a Semiconductor Research Corporation program sponsored by MARCO and DARPA.

## **Author Information**

The authors declare no competing financial interests. Correspondence and requests for materials should be addressed to hyhwang@stanford.edu (H.Y.H.), yicui@stanford.edu (Y.C.).

## References

1. Geim, A. K., Grigorieva, I. V. Van der Waals heterostructures. *Nature* **499**, 419-425 (2013).
2. Wang, Q. H., Kalantar-Zadeh, K., Kis, A., Coleman, J. N., Strano, M. S. Electronics and optoelectronics of two-dimensional transition metal dichalcogenides. *Nature Nanotechnol.* **7**, 699-712 (2012).
3. Novoselov, K. S., Geim, A. K., Morozov, S. V., Jiang, D., Katsnelson, M. I., Grigorieva, I. V., *et al.* Two-dimensional gas of massless Dirac fermions in graphene. *Nature* **438**, 197-200 (2005).
4. Zhang, Y. B., Tan, Y. W., Stormer, H. L., Kim, P. Experimental observation of the quantum Hall effect and Berry's phase in graphene. *Nature* **438**, 201-204 (2005).
5. Novoselov, K. S., Jiang, Z., Zhang, Y., Morozov, S. V., Stormer, H. L., Zeitler, U., *et al.* Room-temperature quantum hall effect in graphene. *Science* **315**, 1379-1379 (2007).
6. Bolotin, K. I., Ghahari, F., Shulman, M. D., Stormer, H. L., Kim, P. Observation of the fractional quantum Hall effect in graphene. *Nature* **462**, 196-199 (2009).
7. Chen, Y. L., Analytis, J. G., Chu, J. H., Liu, Z. K., Mo, S. K., Qi, X. L., *et al.* Experimental Realization of a three-dimensional topological insulator, Bi<sub>2</sub>Te<sub>3</sub>. *Science* **325**, 178-181 (2009).
8. Zhang, H. J., Liu, C. X., Qi, X. L., Dai, X., Fang, Z., Zhang, S. C. Topological insulators in Bi<sub>2</sub>Se<sub>3</sub>, Bi<sub>2</sub>Te<sub>3</sub> and Sb<sub>2</sub>Te<sub>3</sub> with a single Dirac cone on the surface. *Nature Phys.* **5**, 438-442 (2009).
9. Mak, K. F., He, K. L., Shan, J., Heinz, T. F. Control of valley polarization in monolayer MoS<sub>2</sub> by optical helicity. *Nature Nanotechnol.* **7**, 494-498 (2012).
10. Zeng, H. L., Dai, J. F., Yao, W., Xiao, D., Cui, X. D. Valley polarization in MoS<sub>2</sub> monolayers by optical pumping. *Nature Nanotechnol.* **7**, 490-493 (2012).
11. Cao, T., Wang, G., Han, W. P., Ye, H. Q., Zhu, C. R., Shi, J. R., *et al.* Valley-selective circular dichroism of monolayer molybdenum disulphide. *Nature Commun.* **3**, 887 (2012).
12. Li, L. K., Yu, Y. J., Ye, G. J., Ge, Q. Q., Ou, X. D., Wu, H., *et al.* Black phosphorus field-effect transistors. *Nature Nanotechnol.* **9**, 372-377 (2014).
13. Liu, H., Neal, A. T., Zhu, Z., Luo, Z., Xu, X. F., Tomanek, D., *et al.* Phosphorene: an unexplored 2D semiconductor with a high hole mobility. *Acs Nano* **8**, 4033-4041 (2014).
14. Low, T., Rodin, A. S., Carvalho, A., Jiang, Y., Wang, H., Xia, F., Castro Neto, A. H. Tunable optical properties of multilayers black phosphorus thin films. arXiv:1404.4030.
15. Xu, Y., Yan, B. H., Zhang, H. J., Wang, J., Xu, G., Tang, P. Z., *et al.* Large-gap quantum spin Hall insulators in tin films. *Phys. Rev. Lett.* **111**, 136804 (2013).
16. Buscema, M., Groenendijk, D. J., Blanter, S. I., Steele, G. A., Van der Zant, H. S. J., Castellanos-Gomez, A. Fast and broadband photoresponse of few-layer black phosphorus field-effect transistors. *Nano Lett.* **14**, 3347-3352 (2014).

17. Lopez-Sanchez, O., Lembke, D., Kayci, M., Radenovic, A., Kis, A. Ultrasensitive photodetectors based on monolayer MoS<sub>2</sub>. *Nature Nanotechnol.* **8**, 497-501 (2013).
18. Xia, F., Wang, H., Jia, Y. Rediscovering black phosphorus as an anisotropic layered material for optoelectronics and electronics, *Nature Commun.* **5**, 4458 (2014).
19. Qiao, J., Kong, X., Hu, Z. X., Yang, F., Ji, W. High-mobility transport anisotropy and linear dichroism in few-layer black phosphorus. *Nature Commun.* **5**, 4475 (2014).
20. Low, T., Roldán, R., Wang, H., Xia, F., Avouris, P., Moreno, L. M., Guinea, F. Plasmons and screening in monolayer and multilayer black phosphorus. arXiv:1404.4035.
21. Low, T., Engel, M., Steiner, M., Avouris, P., Origin of photoresponse in black phosphorus photo-transistors. arXiv:1407.7286.
22. Fei, R., Faghaninia, A., Soklaski, R., Yan, J. A., Lo, C., Yang, L. Enhanced thermoelectric efficiency via orthogonal electrical and thermal conductances in phosphorene. arXiv:1405.2836.
23. Engel, M., Steiner, M., Avouris, P., A black phosphorus photo-detector for multispectral, high-resolution imaging. arXiv:1407.2534.
24. Buscema, M., Groenendijk, D. J., Steele, G. A., van der Zant, H. S.J., Castellanos-Gomez, A. Photovoltaic effect in few-layer black phosphorus PN junctions defined by local electrostatic gating. arXiv:1407.2863.
25. Deng, Y., Luo, Z., Conrad, N. J., Liu, H., Gong, Y., Najmaei, S., Ajayan, P. M., Lou, J., Xu, X., Ye, P. D. Black phosphorus-monolayer MoS<sub>2</sub> van der Waals heterojunction p-n diode. arXiv:1407.3430.
26. Kamalakar, M.V., Madhushankar, B. N., Dankert, A., Dash, S. P., Engineering Schottky barrier in black phosphorus field effect devices for spintronic applications. arXiv:1406.4476.
27. Dresselhaus, G. Optical absorption band edge in anisotropic crystals. *Phys. Rev.* **105**, 135 (1957).
28. Blakemore J. S., Nomura K. C. Intrinsic optical absorption in Tellurium, *Phys. Rev.* **127**, 1024 (1962).
29. Wang, J. F., Gudiksen, M. S., Duan, X. F., Cui, Y., Lieber, C. M. Highly polarized photoluminescence and photodetection from single indium phosphide nanowires. *Science* **293**, 1455-1457 (2001).
30. Nanot, S., Cummings, A. W., Pint, C. L., Ikeuchi, A., Akiho, T., Sueoka, K., *et al.* Broadband, polarization-sensitive photodetector based on optically-thick films of macroscopically long, dense, and aligned carbon nanotubes. *Sci. Rep.* **3**, 1335 (2013).
31. Liao, Y. L., Zhao, Y. Design of wire-grid polarizer with effective medium theory. *Opt. Quant. Electron.* **46**, 641-647 (2014).
32. Miyamaru, F., Hangyo, M. Polarization response of two-dimensional metallic photonic crystals studied by terahertz time-domain spectroscopy. *Appl. Optics* **43**, 1412-1415 (2004).
33. Guillaumee, M., Dunbar, L. A., Santschi, C., Grenet, E., Eckert, R., Martin, O. J. F., *et al.*

- Polarization sensitive silicon photodiodes using nanostructured metallic grids. *Appl. Phys. Lett.* **94**, 193503 (2009).
34. Han, C. Q., Yao, M. Y., Bai, X. X., Miao, L., Zhu, F., Guan, D. D., Wang, S., Gao, C. L., Liu, C., Qian, D., Liu, Y., Jia, J. F. Electronic structures of black phosphorus studied by angle-resolved photoemission spectroscopy. arXiv:1405.7431.
  35. Lee, M. M., Teuscher, J., Miyasaka, T., Murakami, T. N., Snaith, H. J. Efficient hybrid solar cells based on meso-superstructured organometal halide perovskites. *Science* **338**, 643-647 (2012).
  36. Stranks, S. D., Eperon, G. E., Grancini, G., Menelaou, C., Alcocer, M. J. P., Leijtens, T., *et al.* Electron-hole diffusion lengths exceeding 1 micrometer in an organometal trihalide perovskite absorber. *Science* 342,341-344 (2013).
  37. Jacobs-Gedrim, R. B., Shanmugam, M., Jain, N., Durcan, C. A., Murphy, M. T., Murray, T. M., *et al.* Extraordinary photoresponse in two-dimensional In<sub>2</sub>Se<sub>3</sub> nanosheets. *ACS Nano* **8**, 514-521 (2014).
  38. Cho, J. H., Lee, J., Xia, Y., Kim, B., He, Y. Y., Renn, M. J., *et al.* Printable ion-gel gate dielectrics for low-voltage polymer thin-film transistors on plastic. *Nature Mater.* **7**, 900-906 (2008).
  39. Kawasaki, M., Iwasa, Y. Electronics: 'Cut and stick' ion gels. *Nature* **489**, 510-511 (2012).
  40. Yuan, H. T., Bahramy, M. S., Morimoto, K., Wu, S. F., Nomura, K., Yang, B. J., *et al.* Zeeman-type spin splitting controlled by an electric field. *Nature Phys.* **9**, 563-569 (2013).
  41. Yu, W. J., Liu, Y., Zhou, H. L., Yin, A. X., Li, Z., Huang, Y., *et al.* Highly efficient gate-tunable photocurrent generation in vertical heterostructures of layered materials. *Nature Nanotechnol.* **8**, 952-958 (2013).
  42. Kim, C. O., Kim, S., Shin, D. H., Kang, S. S., Kim, J. M., Jang, C. W., *et al.* High photoresponsivity in an all-graphene p-n vertical junction photodetector. *Nature Commun.* **5**, 3249 (2014).
  43. Liu, C. H., Chang, Y. C., Norris, T. B., Zhong, Z. H. Graphene photodetectors with ultra-broadband and high responsivity at room temperature. *Nature Nanotechnol.* **9**, 273-278 (2014).
  44. Hu, L., Dalgleish, S., Matsushita, M. M., Yoshikawa, H., Awaga, K., Storage of an electric field for photocurrent generation in ferroelectric-functionalized organic devices. *Nature Commun.* **5**, 3279 (2014).
  45. Kresse, G., Hafner, J. Ab initio molecular-dynamics for Liquid-Metals. *Phys. Rev. B* **47**, 558-561 (1993).
  46. Kresse, G., Joubert, D. From ultrasoft pseudopotentials to the projector augmented-wave method. *Phys. Rev. B* **59**, 1758-1775 (1999).
  47. Perdew, J. P., Burke, K., Ernzerhof, M. Generalized gradient approximation made simple. *Phys. Rev. Lett.* **77**, 3865-3868 (1996).

48. Hohenberg, P., Kohn, W. Inhomogeneous Electron Gas. *Phys. Rev. B* **136**, B864 (1964).

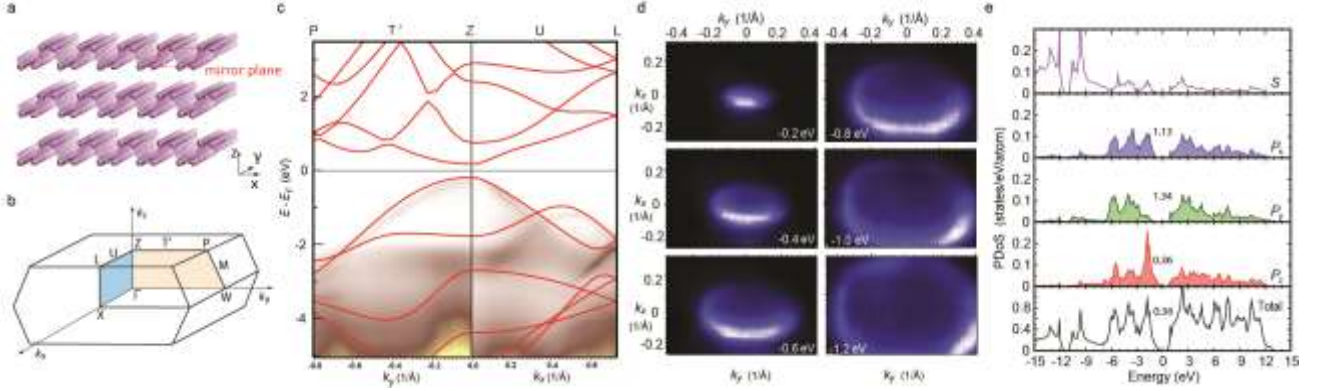


**Figure 1 Anisotropic electronic structure of layered black phosphorus.** **a**, and **b**, Layered crystal structure of black phosphorus and the schematic of its 3D Brillouin zone. The BP lattice shows a novel in-plane atomic buckling along the  $x$ -axis, resulting in a two-fold anisotropy along  $x$  and  $y$  directions, with a direct influence on its band structure and the optical selection rules. The parallelogram plane (red color) in **a** reflects the mirror reflection symmetry in BP structure. **c**, Band structure of cleaved bulk BP, obtained by ARPES measurements (color mapping) and from band calculations (red lines), showing the anisotropic band dispersion and effective mass between Z-P and Z-L directions. **d**, Constant-energy contours show the evolution of the anisotropic band dispersion at different energies from -0.2 eV to -1.2 eV. The energies here are all with respect to the Fermi level. **e**, Partial density of states (PDoS) of BP for  $s$ ,  $p_x$ ,  $p_y$ ,  $p_z$  orbitals. The number in each panel indicates the gap size for each PDoS, where the  $p_z$  orbital along the  $z$  crystal axis contributes all of the band dispersion near the band edge and practically dominates the size of band gap of bulk BP.



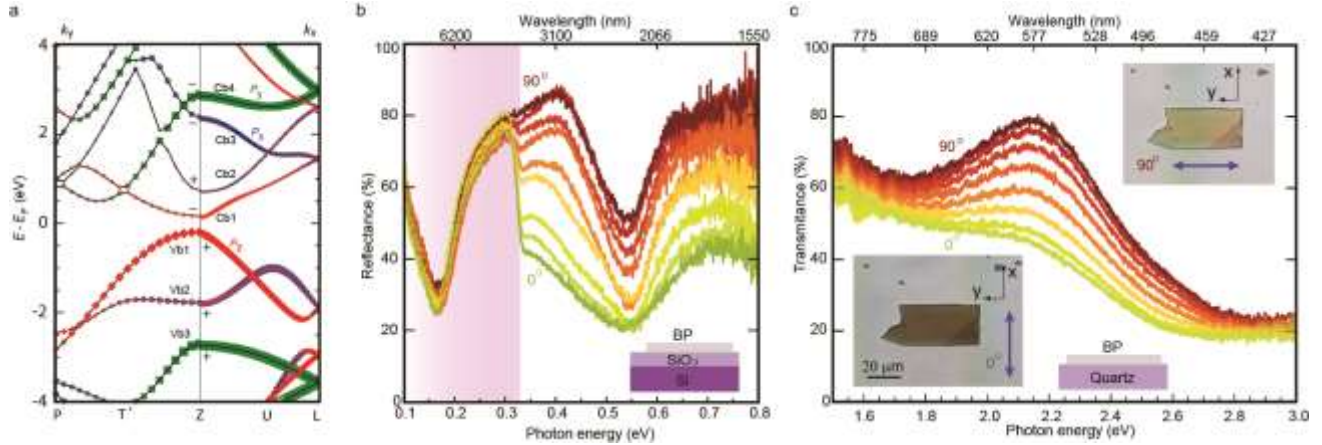


**Figure 2 Optical selection rules and broadband linear dichroism in black phosphorus.** **a**, Orbital component analysis of bulk BP band dispersion. In the Z-L direction, only  $x$ -direction polarized light can be absorbed. In the Z-P direction, light with both  $x$  and  $y$  polarizations can be absorbed. “+” and “-” signals represent the parity of the bands. Red, blue and green colors represent the band dispersion from the  $p_z$ ,  $p_x$ ,  $p_y$  orbitals. **b**, Light polarization dependence of the reflection in the infrared spectral regime, showing around 50% variation in reflection along two perpendicular directions for energies above the band gap (purple shadow area). **c**, Polarization dependence of the transmission of visible light. In both spectra, the incident light is linearly polarized with directions from the  $x$  to the  $y$  crystal axis (from green/ $0^\circ$  to dark-red/ $90^\circ$ ) in  $15^\circ$  steps. The insets in **c** show optical images with incident light along two perpendicular directions (blue arrow represents light polarization direction).

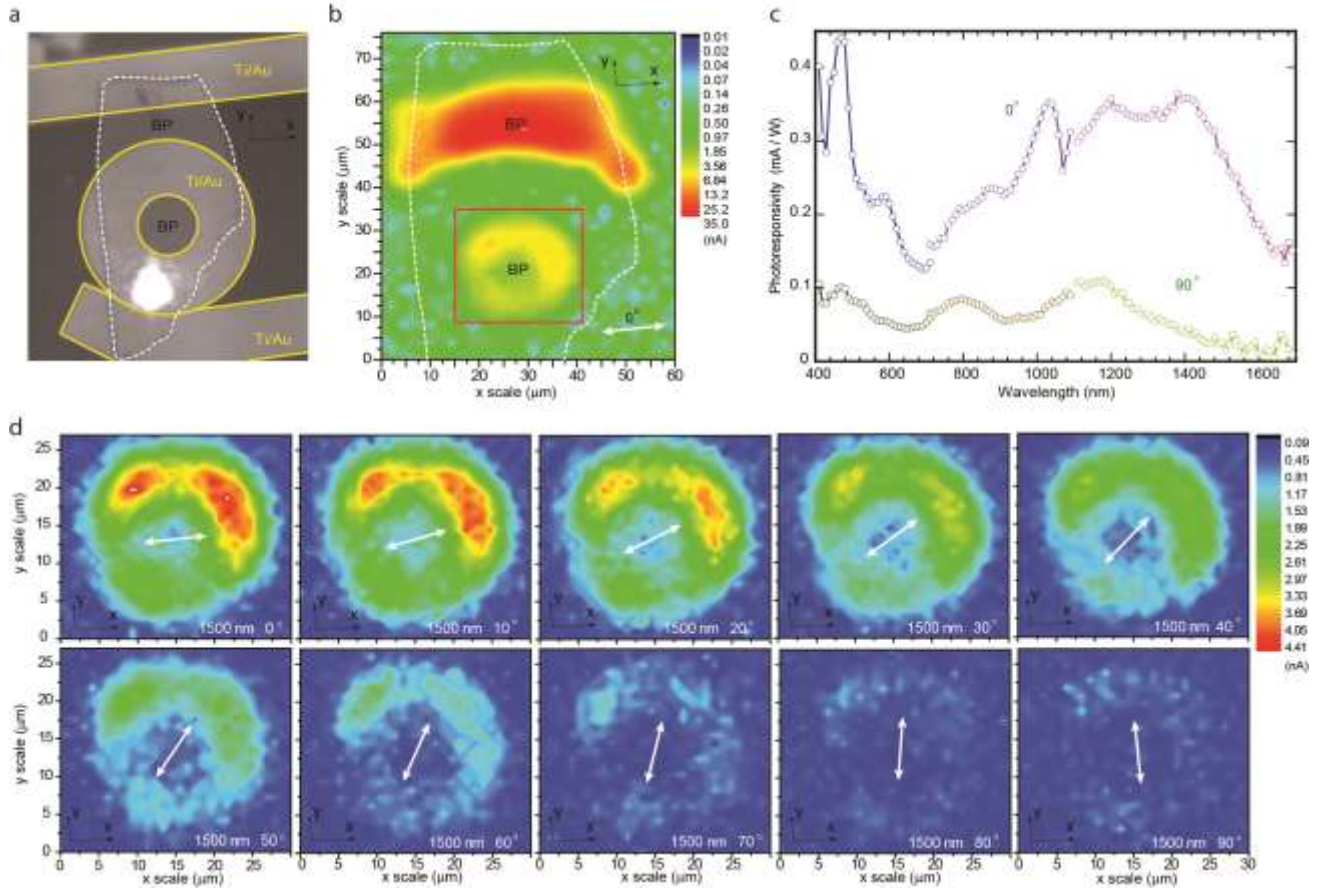


**Figure 3 Black phosphorus photodetector with broadband and polarization sensitivity.** **a**, Optical image of BP photodetector with ring-shaped photocurrent collector. The areas indicating by yellow lines are Ti/Au electrodes and the area circled by white line is the BP flake. In contrast to a “knife”-edge metal electrode, the isotropic round shape photocurrent collector can remove the linear dichroism which might originate from a straight metal edge. **b**, Corresponding photocurrent microscopy images of the device shown in **a**, with illumination at 1500 nm and polarization along the  $x$  direction (white arrow). Further detailed investigations on the photocurrent generation focus on the BP inside the inner ring. **c**, Polarization dependence of the photoresponsivity under illumination from 400 to 1700 nm, where the polarization angle of  $0^\circ$  corresponds to the  $x$  crystal axis while  $90^\circ$  corresponds to  $y$  crystal axis. **d**, Photocurrent microscopy images of the BP inside the inner ring under illumination at 1500 nm with different light polarizations (white arrows reflect the polarization directions). As shown in Supplementary Figs. S5 and S6, similar results are observed under broadband illumination, at least within the spectral regime in our experiment (400 – 1700 nm).

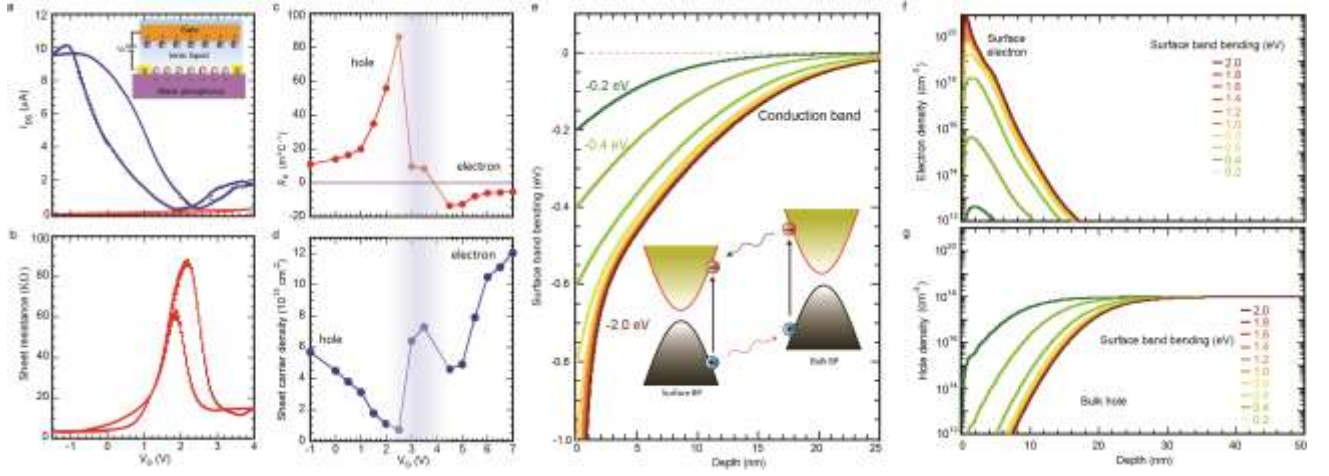


**Figure 4 Ambipolar operation and the vertical p-n junction in BP transistors.** **a**, Ambipolar transfer characteristics in ionic gel gated electric-double-layer transistors based on a cleaved BP flake with a thickness of  $\sim 30$  nm. Inset: Schematic structure of a typical ionic gel gated BP transistor. By applying a gate voltage  $V_G$  to the lateral Au gate electrode, ions in the gel are driven to the BP surface, forming a perpendicular electric field at the BP surface. The blue curve is the source-drain current and the red curve is the corresponding gate current, both measured at 230 K. **b**, Sheet resistance as a function of gate voltage  $V_G$ , indicating an ambipolar behavior similar to graphene transistors. **c**, and **d**, Hall coefficient and sheet carrier density obtained from Hall effect measurements. The maximum attainable sheet carrier densities of  $0.57 \times 10^{14} \text{ cm}^{-2}$  for holes and  $1.2 \times 10^{14} \text{ cm}^{-2}$  for electrons indicate the existence of surface band bending on the BP side. **e**, Self-consistent Poisson-Schrödinger calculations for surface band bending in ionic gel gated BP transistors. Green color represents a weaker downward band bending ( $-0.2$  eV) while dark-red color represents a stronger band bending ( $-2.0$  eV). Inset: schematic diagram of the relative movement of the photogenerated electron/hole pairs in the built-in electric field in a vertical p-n junction. **f** and **g**, Carrier distribution profile in ionic gel gated BP transistors obtained from Poisson-Schrödinger calculations for different band bending (as indicated by the labels), demonstrating the accumulation of electrons on BP surface. Here we use the bulk hole density of  $1 \times 10^{18} \text{ cm}^{-3}$ . A higher bulk carrier density would give a narrower p-n junction (space charge region in the vertical direction) owing to a smaller Thomas-Fermi screening length.

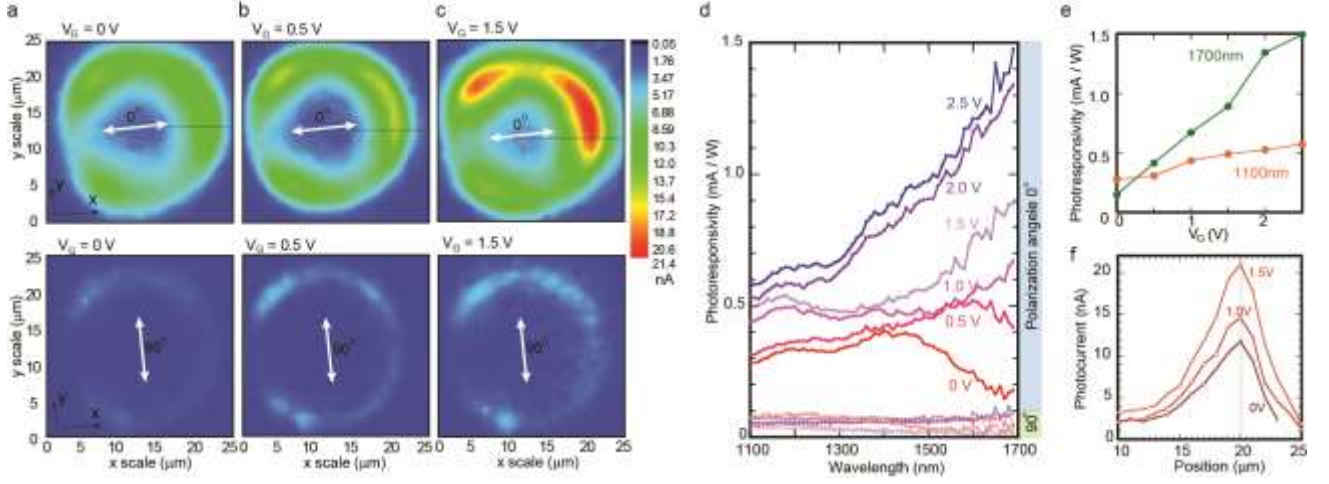


**Figure 5 Gate enhancement of the linear dichroism detection by a vertical p-n junction in a BP electric-double-layer transistor.** **a-c**, Photocurrent microscopy images of the BP device with illumination at  $1500$  nm for two perpendicular polarizations under gate biases  $V_G = 0$  V (**a**),  $0.5$  V (**b**) and  $1.5$  V (**c**). A polarization angle of  $0^\circ$  corresponds to the  $x$  crystal axis while  $90^\circ$  corresponds to the  $y$  crystal axis, as indicated by white arrows. **d**, Gate enhanced linear dichroism detection in BP photodetector as demonstrated by the dependence of the photoresponsivity for incident light polarized along the  $x$  and  $y$  crystal axes. **e**, Gate dependent photoresponsivity at two different wavelengths ( $1100$  nm and  $1700$  nm) for light polarization along the  $x$  axis. **f**, Gate dependent photocurrent profile from the center of the ring to the metal edge along the black dash line shown in panels **a-c**, for light polarization along the  $x$  axis ( $1500$  nm).